

Ultrafine grain formation and coating mechanism arising from a blast coating process: a transmission electron microscopy analysis

**Conor F. Dunne¹, Kevin Roche³, Arne Janssen², Xiangli Zhong², M. G. Burke²,
Barry Twomey^{3*} and Kenneth T. Stanton¹,**

¹UCD School of Mechanical and Materials Engineering, University College Dublin, Belfield,
Dublin 4, Ireland

²Materials Performance Centre and Electron Microscopy Centre, School of Materials, The
University of Manchester, Manchester, U.K.

³ENBIO Ltd., DCU Alpha Innovation Campus, Glasnevin, Dublin 11, Ireland

*Corresponding Author

Email: barrytwomey@gmail.com

Tel: +35315253305

Fax: +35315253309

Keywords: Hydroxyapatite, Transmission electron microscopy, Coating, Ultrafine grain, Steel

Abstract

This article examines the substrate/coating interface of a coating deposited onto mild steel and stainless steel substrates using an ambient temperature blast coating technique known as CoBlast™. The process utilises a co-incident stream of an abrasive blast medium and coating medium particles to modify the substrate surface. The hypothesis for the high bond strength is that the abrasive medium roughens the surface whilst simultaneously disrupting the passivating oxide layer of the substrate, thereby exposing the reactive metal which then reacts with the coating medium. The aim of this study is to provide greater insight into the coating/substrate bonding mechanism by analysing the interface between a hydroxyapatite coating on both mild and stainless steel substrates. The coating adhesion was measured via a tensile test and bond strengths of approximately 45 MPa were measured. The substrate/coating interface was examined using transmission electron microscopy and selected area diffraction. The analysis of the substrate/coating interface revealed the presence of ultrafine grains in both the coating and substrate at interface associated with deformation at the interface caused by particle impaction during deposition. The chemical reactivity resulting from the creation of these ultrafine grains is proposed to explain the high adhesive strength of CoBlast coatings.

1. Introduction

Metals are used in a wide variety of applications due to their high strength, resistance to fracture, high ductility, and toughness. However, particularly in the medical device sector, they do not possess all the requisite surface properties for their required application, and so coatings may be applied to address this [1]–[3]. More broadly, ceramic coatings have been applied to metal substrates to provide protection from a variety of degradation processes such as wear, corrosion, biological and thermal attack [4].

Thermal coating techniques, in particular plasma spraying, are commonly used for depositing ceramic coatings onto metals [5], [6]. There are a number of problems associated with high temperature coating techniques, such as the formation of unwanted phases, decomposition of and amorphisation of the coating material, or poor adherence of the coating [7], [8]. Although Cold Spray has been investigated for the deposition of bioceramics, it is typically used in conjunction with a metal phase such as titanium to bond or hold the ceramic in place [9].

This present work examines the bonding mechanism for an alternative deposition technique – CoBlast™. CoBlast is an ambient temperature and pressure blast coating technique and is capable of depositing highly-adherent, thin coatings, with minimal phase modification of the deposited material. Hydroxyapatite (HA, $\text{Ca}_5(\text{PO}_4)_3(\text{OH})$) coatings with bond strengths ≈ 60 MPa have been reported for titanium substrates compared to ≈ 20 MPa for plasma sprayed hydroxyapatite coatings [8], [10], [11]. The process utilises a co-incident stream of an abrasive blast medium and a stream of coating medium particles to modify the substrate surface. The hypothesis for the high bond strength is that abrasive roughens the surface whilst simultaneously disrupting the passivating oxide layer of the substrate, thereby exposing the reactive metal. The stream of coating medium then reacts with the exposed reactive metal to form an intimate chemical bond at the interface, giving rise to high bond strengths [8], [10], [11].

The formation of a gradient nano-grained (GNG) surface structure attributed to, amongst other things, high-strain rates, has been used to describe a transition from nano-grained surface layers with an increase in grain size into the bulk substrate [12]. The CoBlast process is not expected to generate the same high strain rates observed in Cold Spray due to a reduced operating pressure and resultant particle velocity i.e. < 250 m/s at room temperature [13]. However, the presence of GNG formation during the CoBlast process may explain the high apparent bond strengths. Previously, severe plastic deformation (SPD) up to 20 and 35 μm into the surface of Grade 2 or commercially pure titanium has been observed in substrates coated using CoBlast [8], [10]. SPD has been shown to give rise to the formation of ultrafine grains by introducing high dislocation densities that subsequently rearrange into high angle grain boundaries with submicron grain sizes [14]–[17] whereas shot peening has been shown to produce nanocrystalline surface layers [18], [19]. Examination of the interface may provide insight into

whether SPD gives rise to a GNG surface as smaller grains exhibit greater reactivity per unit volume than larger particles [20]–[22].

The present study investigates the phenomenon of ultra-fine grain formation in both the metallic substrate and ceramic coating in the CoBlast process. This may provide an insight into the proposed mechanism of bond formation between the coating and substrate and subsequent high coating adhesion observed. The substrate/coating pair of mild steel and hydroxyapatite as used here constitutes a model system for the purposes of the present study and no end application of this pair is proposed as mild steel would not be used in medical devices. Mild steel presents a simpler interface system to the alloyed 316 stainless steel. The reactivity of hydroxyapatite and its applicability with the CoBlast technique has been previously described on other substrates including titanium [8], magnesium [23] and nitinol [24].

2. Materials and methods

2.1. Materials

Mild steel (SAE 1008) (Impact Ireland Metals, Ireland) and stainless steel (SAE 316) (Impact Ireland Metals) were used as the substrates in this study. Five coupons ($15 \times 15 \times 1$ mm) of each alloy were coated per set. Hydroxyapatite (HA, $\text{Ca}_5(\text{PO}_4)_3(\text{OH})$) was used as the coating medium. The HA (SAI, France) particle size used was 25–60 μm . Alumina (White Saftigrit, grade F240 or $< 50 \mu\text{m}$, Guyson USA) was used as the blast medium. Figure 1 shows scanning electron microscopy (SEM) images of the coating and abrasive blast media.

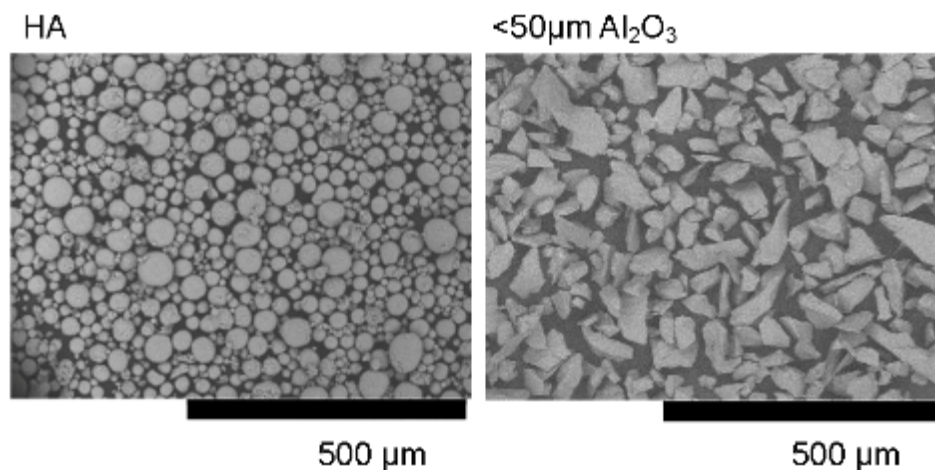


Figure 1: Backscattered electron images of HA and alumina powders.

2.2. Coating Procedure

The coupons were placed on a stationary tray and treated using CoBlast to produce a HA layer on the surface. Figure 2 shows a schematic of the coating process.

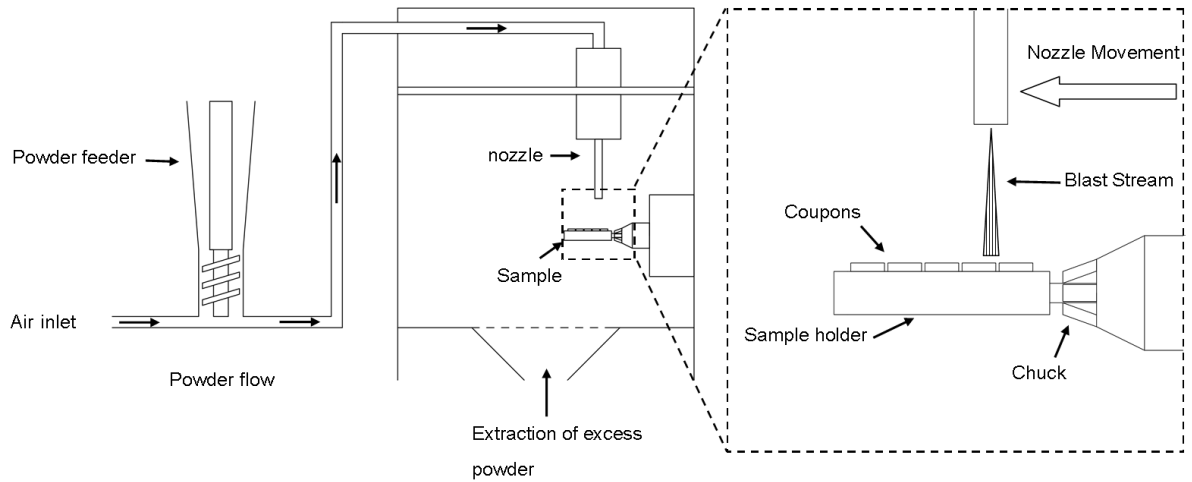


Figure 2: Schema of coupon coating process.

2.3. Surface characterisation

Energy Dispersive X-ray (EDX) spectrum imaging was performed on the surface of the substrates before and after coating to examine coating coverage using a FEI Quanta 3D FEG DualBeam Focused Ion Beam (FIB) (FEI Ltd, Hillsboro, USA) operated at 15 kV and equipped with an EDAX EDX APOLLO XV Silicon Drift Detector.

The surface roughness of the coated and as-supplied mild steel and stainless steel coupons was measured using a Nanovea PS50 optical profilometer (Nanovea, Irvine, CA, USA). The average profile height (R_a) and maximum profile height (R_z) were measured over 1 mm lengths for each coupon.

2.4. Coating adhesion

Tensile bond strength tests were carried using a modified version of the method given in the ASTM F1147-05 [34]. Epoxy-coated 2.7 mm diameter aluminium studs (Quad Group Inc., USA) were fixed and cured to the coated surfaces for 1 hour at 150 °C and then left to cool to room temperature. The bond strength (Force/Area) was determined by measuring the force required to remove the stud from the surface using a Sebastian 5 Pull Tester (Quad Group, Washington, U.S.A.) using a displacement rate of 2.5 mm/min. This configuration is deemed to be more suitable for smaller surfaces and thin coatings as the glue penetration has less of an effect on the test and repeat measurements can be taken on the same sample in a different area to ensure repeatability of the results.

2.5. FIB Specimen Preparation

The TEM specimen preparation was performed using the “lift-out” technique using a FEI Helios 660 NanoLab Ga⁺ dual beam FIB (FEI Ltd, Hillsboro, USA). After depositing a protective layer of Pt over the region of interest, the TEM samples were then “cut out” from

the bulk material, using the Ga ion beam and placed on a Cu support grid for subsequent FIB “thinning” to produce an electron-transparent sample.

2.6 . TEM Characterisation

TEM analyses were performed using an FEI Tecnai T20 analytical electron microscope (FEI Ltd, Hillsboro, USA) operating 200 keV and equipped with a LaB₆ cathode. EDX analyses (spectra and spectrum image datasets) were acquired in STEM mode with the Oxford Instruments X-Max^N 80TLE windowless Silicon Drift Detector (SDD) and Aztec analysis system.

3. Results

3.1. Surface Characterisation

The average surface roughness values (R_a and R_z) are shown in Table 1. The CoBlast process gave rise to an average profile height R_a of approximately 1 μm on both steel and mild steel, despite each substrate having a different starting roughness, due to the process-driven action of removing the existing profile and creating a new profile. The roughness of the stainless steel sample is slightly lower, which can be attributed to the higher hardness of the stainless steel (160HV30) compared to mild steel (98HV30).

Table 1: Surface roughness of as-supplied and coated substrates

| | Average profile height R_a (μm) | Maximum profile height R_z (μm) |
|-----------------------------------|---|---|
| Mild steel (as-supplied) | 1.40 | 12.00 |
| Mild steel (coated) | 1.08 | 6.51 |
| | | |
| 316 stainless steel (as-supplied) | 0.58 | 3.23 |
| 316 stainless steel (coated) | 0.82 | 5.08 |

The surface morphology of the substrates before and after surface modification are shown in the SEM images of Figure 3. The substrates exhibited good coating coverage with little of the underlying substrate visible. The substrate appears as brighter regions in the backscattered electron images (B) in thin coating regions and areas of low coating coverage. Elemental images for Ca and P extracted from the EDX spectral image dataset of the substrate surface

confirmed the presence of Ca and P on the surface corresponding to hydroxyapatite, which confirmed good coating coverage.

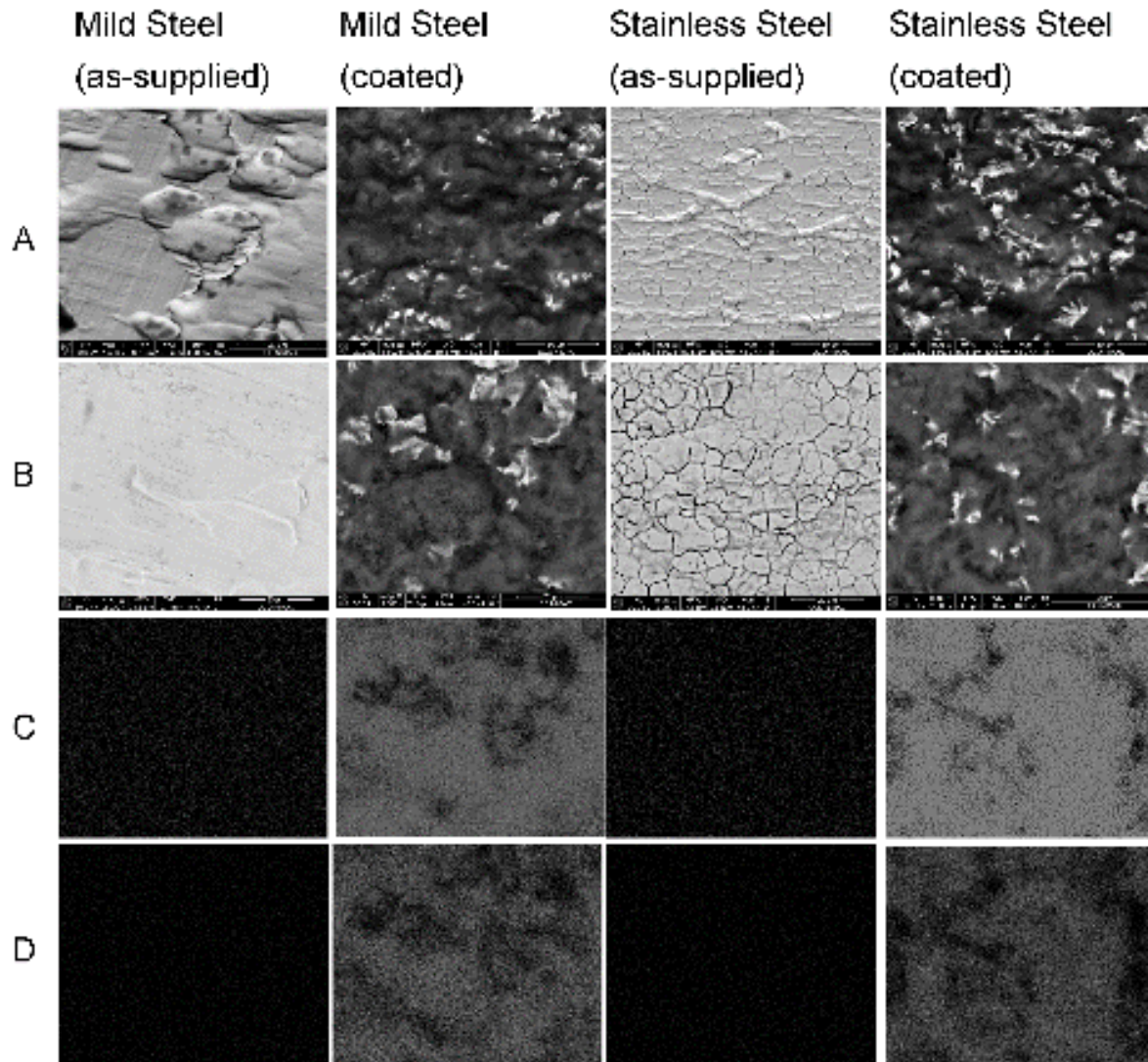


Figure 3: SEM images of the surface and EDX spectral images of the as-supplied and coated substrates. (A) Secondary electron images of coated surfaces at a tilt of 45 °, (B) Backscattered electron images of flat substrates, (C) EDX Ca elemental image and (D) EDX P elemental image extracted from the spectrum image dataset.

3.2. Coating adhesion

Figure 4 shows the tensile bond strength of the HA coatings on each of the coupons. Five measurements were undertaken for each substrate type. Previous measurements on titanium substrates with bond strengths in this range (≈ 57 MPa) exhibited a cohesive failure with adhered HA observed on both the adhesive stud and substrate with a reduction in the EDX

elemental concentration measured on the substrate after testing [8]. Complete coating removal would present as a significant decrease in bond strength.

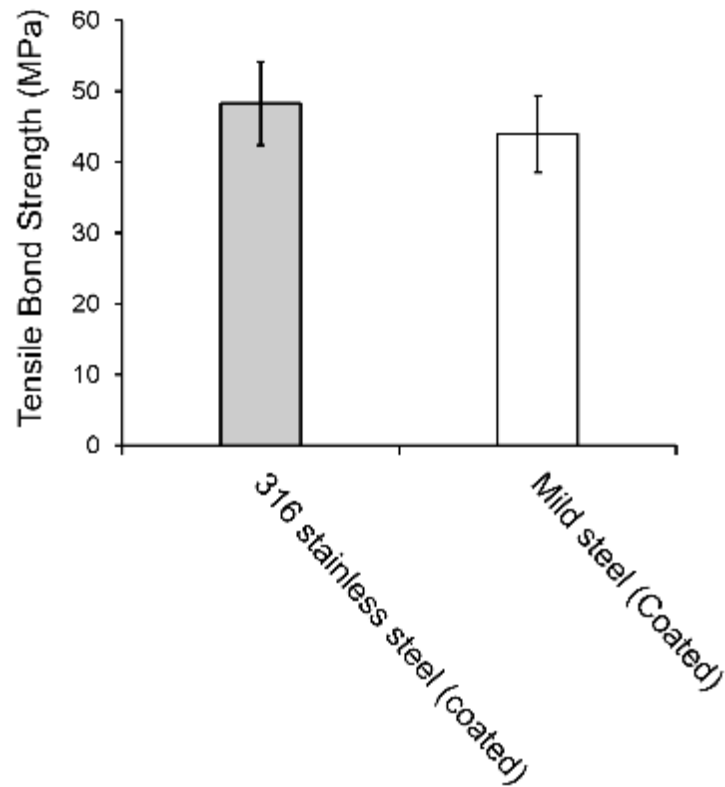


Figure 4: Tensile bond strength of coating on both substrates (scale bar represents standard deviation).

3.3. TEM Analysis

Figure 5 shows a TEM cross-section of the HA coating on the mild steel. The substrate exhibited asperity peaks, with valleys between them: the coating mostly fills in these valleys and is deposited in a thinner layer on the peaks. The coating varied from being very dense in areas with no individual particles visible to areas where coarser packed particles can be easily discerned. The interface between the coating and the substrate is clearly visible and appeared to be very solid and free of voids or other flaws in most areas.

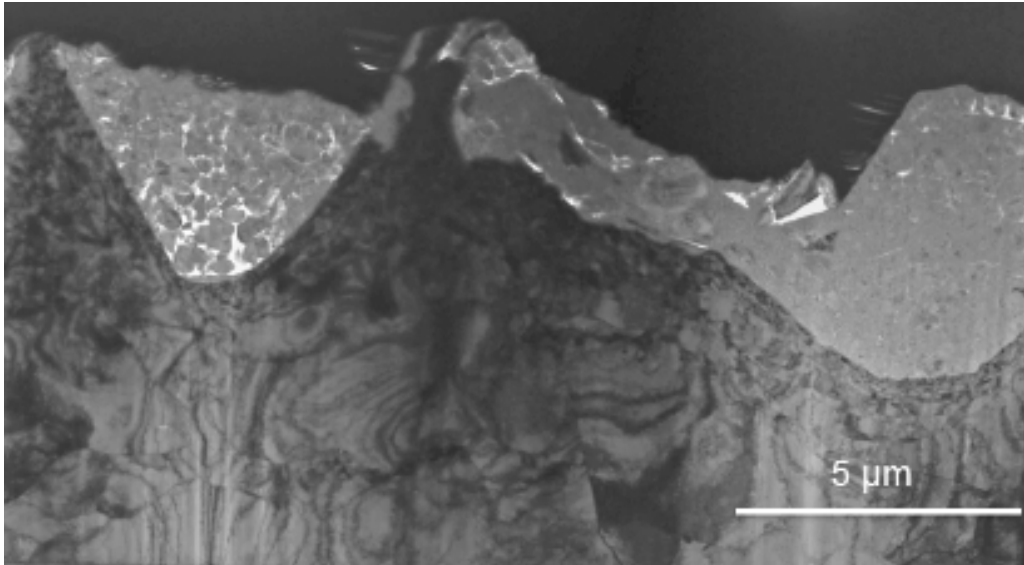


Figure 5: TEM montage of FIB cross-section of CoBlast HA on mild steel substrate.

A contiguous interface is shown by the higher magnification TEM examination of the interface in Figure 6. A distinct delineation between substrate and coating was observed, and there was no evidence of an intermediate interfacial layer. This is supported by the EDX analyses; spectrum A shows only HA elements (Ca, P and O) whereas spectrum B shows only mild steel elements (Fe). The copper in each spectrum is from the sample support grid.

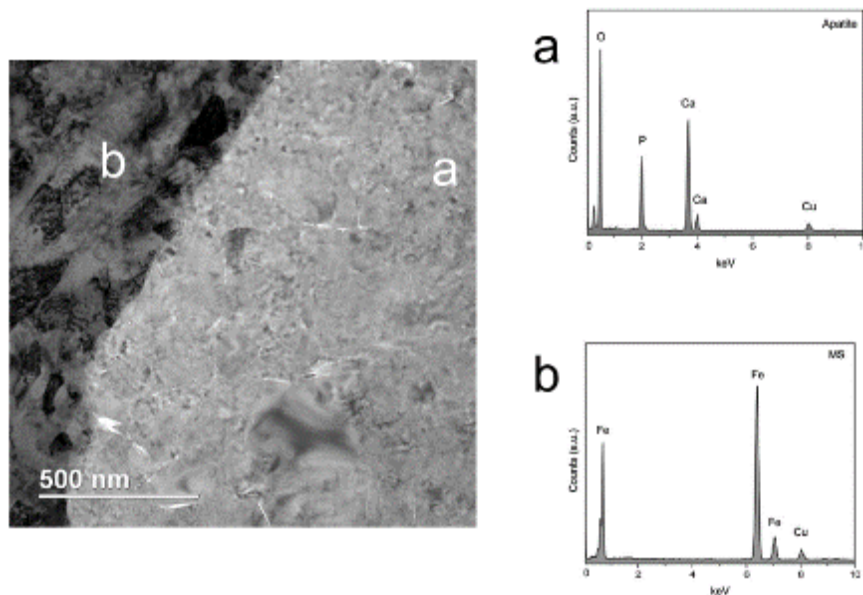


Figure 6: TEM image of the cross-section and corresponding EDX spectra from the HA coating and the mild steel substrate.

Figure 7 shows the interface at the nanoscale. At this magnification there is still no evidence of phases other than the substrate and coating. The substrate was characterized by the presence of ultrafine grains adjacent to the interface whereas in Figure 7(b) lattice fringes corresponding to the (100) plane of HA were visible with a spacing of approximately 0.9 nm. The grain size of the HA coating was several tens of nanometres.

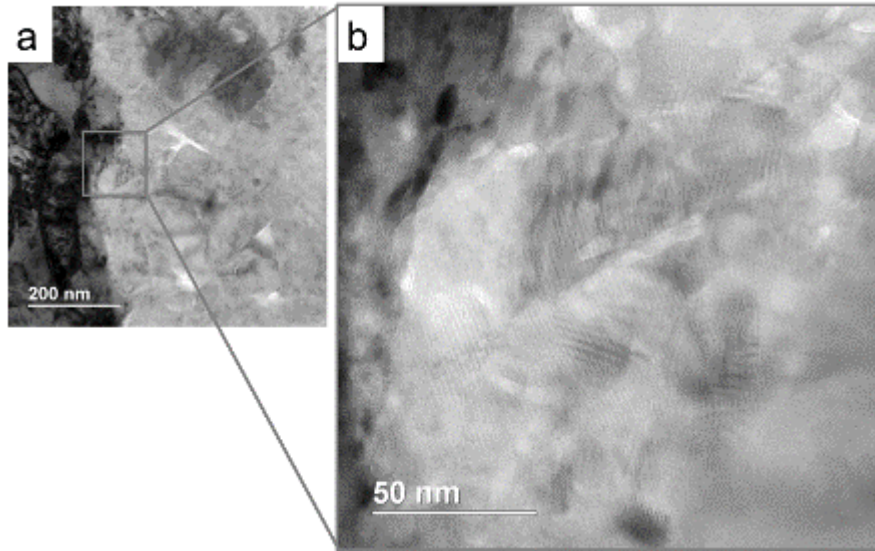


Figure 7: Higher magnification TEM image of the interface between the HA coating (light grey) and mild steel substrate (dark grey).

TEM characterisation of the stainless steel sample showed similar features to those of the mild steel with some additional features to note. The overview cross-section of the stainless steel sample, Figure 8, exhibited similar asperities and valleys on the substrate surface that were “smoothed over” by the coating, and a generally densely packed HA coating. A large alumina inclusion near the left edge of Figure 8 and a smaller alumina inclusion and void just right of the centre of the image were also observed in this sample.

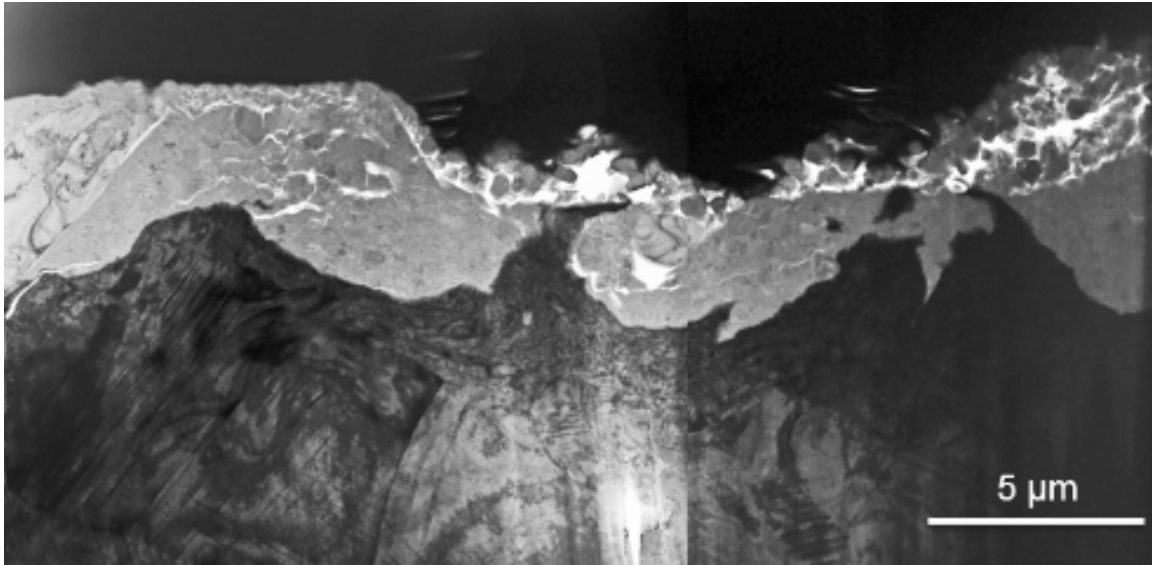


Figure 8: TEM montage of FIB-cut cross-section of CoBlast HA on stainless steel substrate.

Figure 9 gives a higher magnification view of the smaller alumina inclusion with corresponding EDX spectra of the (a) the HA coating, (b) the alumina inclusion, and (c) the substrate. Each phase is clearly identified by the EDX spectra. Spectrum A shows only HA elements, i.e. Ca and P, and copper, spectrum B shows only alumina elements and copper (again, from the TEM grid), and C shows only steel elements, copper, and small amounts of Ca and P due to the proximity of the analysis area to the interface with the coating.

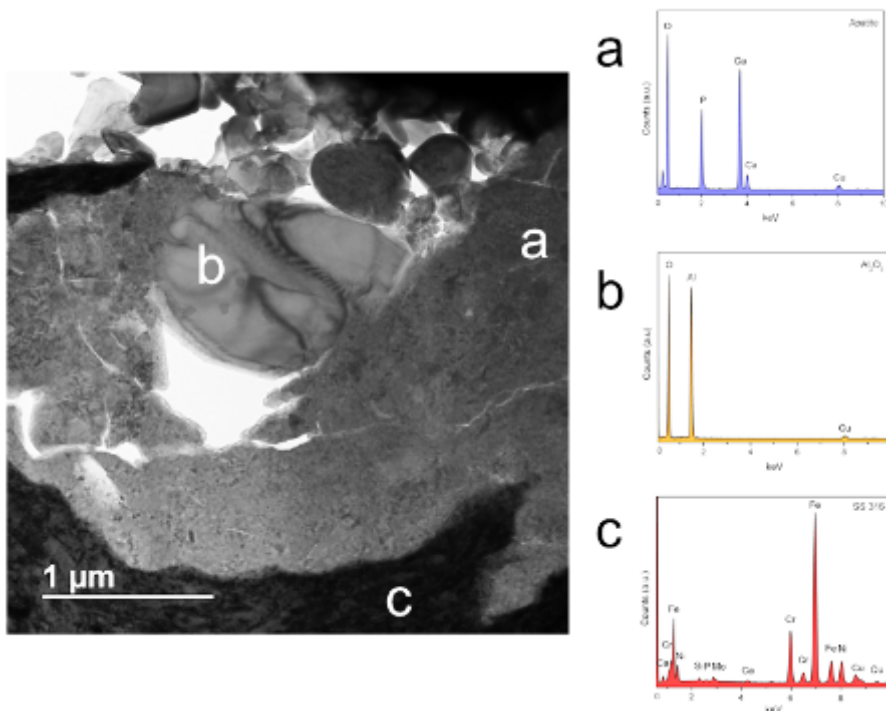


Figure 9: TEM image of the FIB-prepared coating cross-section and corresponding EDX spectra for HA coating, alumina abrasive inclusion, and stainless steel substrate.

In Figure 10, the Selected Area Electron Diffraction Pattern (SADP) of a clearly visible single particle of HA near the outer surface of the coating (Fig. 10 a and b) and a densely packed area near the inner surface of the coating (Fig. 10 a and b). The SADP obtained from the single particle (Figure 10b) indicated that it was a single crystal of HA, whereas the combination of the “spotty” rings and some discrete reflections in the SADP of Figure 10d indicated that the densely packed area was composed primarily of fine-grained, nanoscale crystals and some coarser crystals.

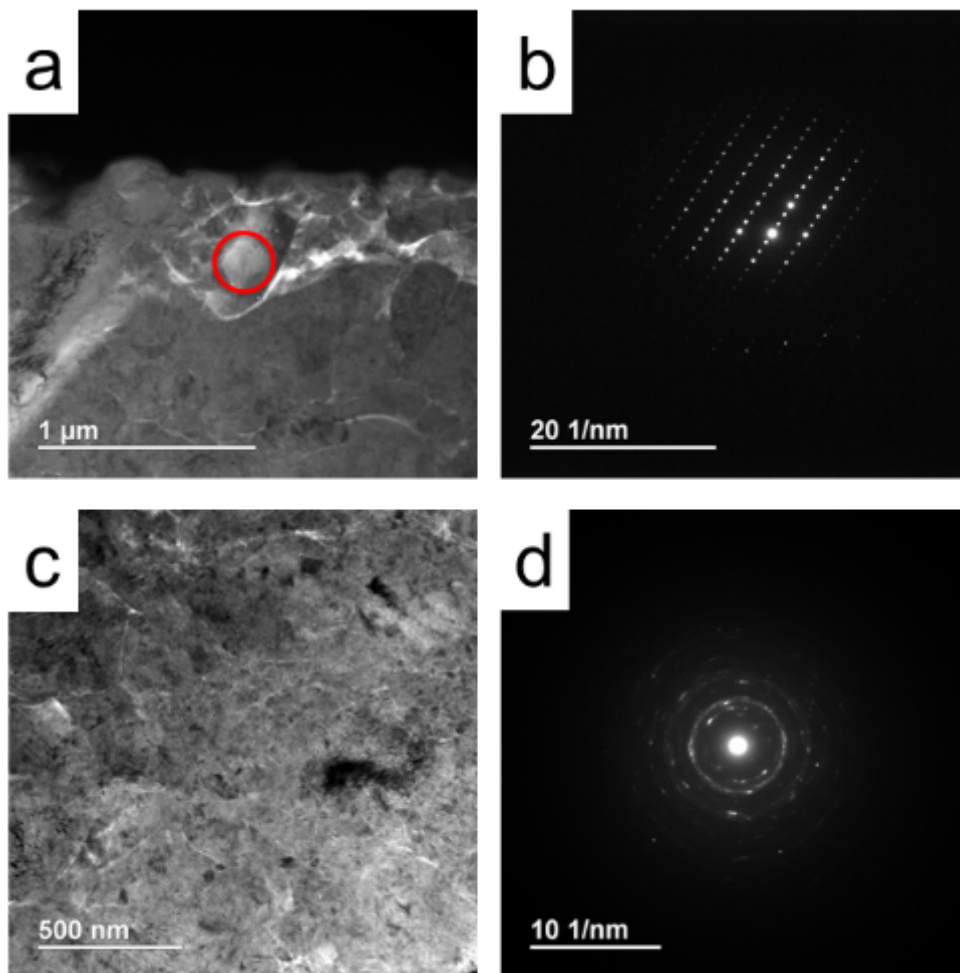


Figure 10: a,b) Selected area electron diffraction pattern (SADP) of the relatively large single crystal of HA indicated by the red circle in ‘a’ , located near the outer edge of the coating. c,d) SADP of densely-packed nano-grained HA close to the interface between the coating and the substrate.

4. Discussion

While exhibiting similar underlying chemistry, mild steel and stainless steel present different obstacles to successful coating with the presence of surface oxides (FeO) and passivating layers (CrO) respectively. This difference provides a good model application for investigating the bond mechanism of the CoBlast process using a well understood material such as HA.

The cross-sections of the two substrates, Figure 5 and Figure 8, showed a variation in coating density along the surface. The density of the coating also appeared to vary with distance from the substrate surface, with a dense coating adjacent to the substrate while coarser particles were visible further away from the interface.

Both the substrate and HA exhibited ultrafine grains at the coating/substrate interface, shown in Figure 7. In the substrate, these were formed due to severe plastic deformation during the blasting process. Similar ultrafine grains have been observed by Zhang et al. in equal-channel angular pressing of mild steel [16] and severe mechanical attrition of stainless steel [17]. This severe deformation or SPD and grain refinement may enhance the reactivity of the surface as the presence of these microstructures along with the associated increase in dislocation density and vacancy concentration [12], [18], [25], [26]. The increase in grain boundary area per unit volume and dislocation density due to SPD has been identified as an explanation for synthesis of compounds during ball milling [27], [28]. These structures store large amounts of energy in the grain boundaries and grain interior [14]. For example, the greater corrosion resistance of ultrafine grain Ti compared to coarse-grained Ti has been attributed to the greater in dislocation density of ultrafine-grained Ti promoting the rapid formation of the passivating film [25].

Figure 7b and Figure 10 c,d showed the presence of nanograined HA at the substrate interface for both the mild steel and stainless steel whereas away from the substrate (Figure 10a,b) coarser particles of HA were detected. The formation of these HA nanograins at the substrate surface may be due to the impact of the particle on the substrate surface and simultaneous bombardment by alumina particles resulting in the fracture of the particles with concomitant increase of total surface area per unit volume. These newly-created surfaces are likely to contain an increased density of chemically-active dangling bonds similar to those generated during the ball milling process [27], [29]–[31]. After ball milling, nanoparticles have been shown to have greater reactivity than larger particles [32, 33]. The presence of these ultrafine or nano-grain structure gradients (GNGs) within both the substrate and HA coating media highlight the severe deformation (SPD in the case of the metal) occurring during the process on both sides of the interface.

As the abrasive and HA are sprayed simultaneously, the formation of both the ultrafine grains in the substrate and nano-grains with the HA must occur concurrently. Thus, the newly-formed HA surfaces with chemically-active dangling bonds are in intimate contact with the reactive ultrafine grains in the metallic substrate. Although the exact bond nature is beyond the scope of the present study, the presence of ultrafine and/or nano-grained structures, and lack of interface or passivating layer, are favourable for a primary chemical bond formation at the interface and explains the subsequent high mechanical bond strengths measured with CoBlasted coatings.

5. Conclusions

Hydroxyapatite was deposited onto mild steel and stainless steel coupons using the CoBlast process of simultaneous blasting of coating and abrasive particles at room temperature. Microstructural examination of the coating has revealed the presence of ultrafine and nano-grains in both the coating and substrate at the interface most likely due to severe deformation at the interface between the substrate and coating media. In the case of the metal surfaces, severe plastic deformation occurred. Little morphological difference was observed between the HA coatings produced on either substrate, and are similar to previous described coatings produced on titanium and magnesium alloys, indicating the process is not necessarily substrate sensitive. The increased chemical activity resulting from the creation of these ultrafine grains is proposed to explain the chemical bonding mechanism and high adhesive strength of CoBlast coatings.

6. Acknowledgement

This study was part funded by the Programme for Research in Third-Level Institutions (PRTL) research number: R12662.

7. References

- [1] R. Narayan, *Biomedical Materials*. New York, U.S.A: Springer, 2009.
- [2] M. Driver, *Coatings for biomedical applications*. Woodhead, 2013.
- [3] M. Moravej and D. Mantovani, 'Biodegradable metals for cardiovascular stent applications: interests and new opportunities', *Int. J. Mol. Sci.*, vol. 12, no. 7, pp. 4250–4270, 2011.
- [4] R. B. Heimann, *Plasma-spray coating: principles and applications*. John Wiley & Sons, 2008.
- [5] Y. Wang, S. Jiang, M. Wang, S. Wang, T. D. Xiao, and P. R. Strutt, 'Abrasive wear characteristics of plasma sprayed nanostructured alumina/titania coatings', *Wear*, vol. 237, no. 2, pp. 176–185, 2000.
- [6] M. Cadenas, R. Vijande, H. J. Montes, and J. M. Sierra, 'Wear behaviour of laser clad and plasma sprayed WC-Co coatings', *Wear*, vol. 212, no. 2, pp. 244–253, 1997.
- [7] C. F. Dunne, J. Gibbons, D. P. FitzPatrick, K. J. Mulhall, and K. T. Stanton, 'On the fate of particles liberated from hydroxyapatite coatings in vivo', *Ir. J. Med. Sci.* 1971-, pp. 1–9, 2015.

- [8] C. F. Dunne, B. Twomey, L. O'Neill, and K. T. Stanton, 'Co-blasting of titanium surfaces with an abrasive and hydroxyapatite to produce bioactive coatings: Substrate and coating characterisation', *J. Biomater. Appl.*, vol. 28, pp. 767–778, Jan. 2014.
- [9] X. Zhou, Pravansu Mohanty, 'Electrochemical behavior of cold sprayed hydroxyapatite/titanium composite in Hanks' solution', *Electrochimica Acta*, 65, pp. 134-140, 2012
- [10] C. F. Dunne, B. Twomey, C. Kelly, J. C. Simpson, and K. T. Stanton, 'Biological response to hydroxyapatite and fluorapatite coated dental screws', *J. Mater. Sci. Mater. Med.*, vol. 26, no. 22, 2015.
- [11] C. F. Dunne, B. Twomey, and K. T. Stanton, 'Effect of a blast coating process on the macro and microstructure of grade 5 titanium foam', *Mater. Lett.*, 2015.
- [12] R. Thevamaran, O. Lawal, S. Yazdi, S.-J. Jeon, J.-H. Lee, E. L. Thomas, 'Dynamic creation and evolution of gradient nanostructure in single-crystal metallic microcubes', *Science*, 354 (6310), pp. 312-316, 2016
- [13] C. Stenson, M. Meyer, B. Twomey and R. Lupoi, 'Particle speed analysis in CoBlast', *Procedia CIRP*, 37, 77-82, 2015
- [14] H. Mughrabi, H. W. Hoppel, and M. Kautz, 'Fatigue and microstructure of ultrafine-grained metals produced by severe plastic deformation', *Scr. Mater.*, vol. 51, no. 8, pp. 807–812, 2004.
- [15] Y. Huang and T. G. Langdon, 'Advances in ultrafine-grained materials', *Mater. Today*, vol. 16, no. 3, pp. 85–93, 2013.
- [16] L. Zhang, A. Ma, J. Jiang, D. Yang, D. Song, and J. Chen, 'Sulphuric acid corrosion of ultrafine-grained mild steel processed by equal-channel angular pressing', *Corros. Sci.*, vol. 75, pp. 434–442, 2013.
- [17] H. W. Zhang, Z. K. Hei, G. Liu, J. Lu, and K. Lu, 'Formation of nanostructured surface layer on AISI 304 stainless steel by means of surface mechanical attrition treatment', *Acta Mater.*, vol. 51, no. 7, pp. 1871–1881, 2003.
- [18] S. Bagheri and M. Guagliano, 'Review of shot peening processes to obtain nanocrystalline surfaces in metal alloys', *Surf. Eng.*, vol. 25, no. 1, pp. 3–14, 2009.
- [19] Y.G. Liu, M.Q. Li, H.J. Liu, 'Nanostructure and surface roughness in the processed surface layer of Ti-6Al-4V via shot peening', *Materials Characterization*, 123, pp. 83-90, 2017
- [20] G. Skandan, H. Hahn, M. Roddy, and W. R. Cannon, 'Ultrafine-Grained Dense Monoclinic and Tetragonal Zirconia', *J. Am. Ceram. Soc.*, vol. 77, no. 7, pp. 1706–1710, 1994.

- [21] Z. Zhang, C.-C. Wang, R. Zakaria, and J. Y. Ying, 'Role of particle size in nanocrystalline TiO₂-based photocatalysts', *J. Phys. Chem. B*, vol. 102, no. 52, pp. 10871–10878, 1998.
- [22] K. Lu and J. Lu, 'Nanostructured surface layer on metallic materials induced by surface mechanical attrition treatment', *Mater. Sci. Eng. A*, vol. 375, pp. 38–45, 2004.
- [23] C. Dunne, G.K. Levy, O. Hakimi, E. Eghion, B. Twomey and K. T. Stanton, 'Corrosion behaviour of biodegradable magnesium alloys with hydroxyapatite coating', *Surface and Coatings Technology*, 289, pp. 37-44, 2016
- [24] C. F. Dunne; K. Roche; B. Twomey and K. T Stanton, 'Deposition of hydroxyapatite onto shape memory NiTi wire', *Materials Letters*, 176, pp. 185-188, 2016
- [25] A. Balyanov, J. Kutnyakova, N. A. Amirkhanova, V. V. Stolyarov, R. Z. Valiev, X. Z. Liao, Y. H. Zhao, Y. B. Jiang, H. F. Xu, and T. C. Lowe, 'Corrosion resistance of ultra fine-grained Ti', *Scr. Mater.*, vol. 51, no. 3, pp. 225–229, 2004.
- [26] M. J. Zehetbauer and Y. T. Zhu, *Bulk nanostructured materials*. John Wiley & Sons, 2009.
- [27] T. Xing, J. Sunarso, W. Yang, Y. Yin, A. M. Glushenkov, L. H. Li, P. C. Howlett, and Y. Chen, 'Ball milling: a green mechanochemical approach for synthesis of nitrogen doped carbon nanoparticles', *Nanoscale*, vol. 5, no. 17, pp. 7970–7976, 2013.
- [28] H. J. Fecht, E. Hellstern, Z. Fu, and W. L. Johnson, 'Nanocrystalline metals prepared by high-energy ball milling', *Metall. Trans. A*, vol. 21, no. 9, pp. 2333–2337, 1990.
- [29] G. Kaupp, 'Mechanochemistry: the varied applications of mechanical bond-breaking', *CrystEngComm*, vol. 11, no. 3, pp. 388–403, 2009.
- [30] S. L. James, C. J. Adams, C. Bolm, D. Braga, P. Collier, T. Friscic, F. Grepioni, K. D. M. Harris, G. Hyett, and W. Jones, 'Mechanochemistry: opportunities for new and cleaner synthesis', *Chem. Soc. Rev.*, vol. 41, no. 1, pp. 413–447, 2012.
- [31] Y. Chen, T. Halstead, and J. S. Williams, 'Influence of milling temperature and atmosphere on the synthesis of iron nitrides by ball milling', *Mater. Sci. Eng. A*, vol. 206, no. 1, pp. 24–29, 1996.
- [32] A. J. Zarur and J. Y. Ying, 'Reverse microemulsion synthesis of nanostructured complex oxides for catalytic combustion', *Nature*, vol. 403, no. 6765, pp. 65–67, 2000.
- [33] N. P. Rao, H. J. Lee, M. Kelkar, D. J. Hansen, J. V. R. Heberlein, P. H. McMurry, and S. L. Girshick, 'Nanostructured materials production by hypersonic plasma particle deposition', *Nanostructured Mater.*, vol. 9, no. 1, pp. 129–132, 1997.

List of Figures

Figure 1: Backscattered electron images of HA and alumina powders.

Figure 2: Schema of coupon coating process.

Figure 3: SEM images of the surface and EDX spectrum images of the as-supplied and coated substrates. (A) Secondary electron images of coated surfaces at a tilt of 45° , (B) Backscattered electron images of flat substrates, (C) EDX spectrum image of Ca and (D) EDX spectrum image of P

Figure 4: Tensile bond strength of coating on both substrates.

Figure 5: TEM montage of FIB cross-section of CoBlast HA on mild steel substrate.

Figure 6: TEM image of the cross-section and corresponding EDX spectra from the HA coating and the mild steel substrate.

Figure 7: Higher magnification TEM image of the interface between the HA coating (light grey) and mild steel substrate (dark grey).

Figure 8: TEM montage of FIB-cut cross-section of CoBlast HA on stainless steel substrate.

Figure 9: TEM image of the FIB-prepared coating cross-section and corresponding EDX spectra for HA coating, alumina abrasive inclusion, and stainless steel substrate.

Figure 10: a,b) Selected area electron diffraction pattern (SADP) of the relatively large single crystal of HA indicated by the red circle in 'a', located near the outer edge of the coating. c,d) SADP of densely-packed nano-grained HA close to the interface between the coating and the substrate.

Table 1: Surface roughness of as-supplied and coated substrates

| | Average profile height R_a (μm) | Maximum profile height R_z (μm) |
|-----------------------------------|---|---|
| Mild steel (as-supplied) | 1.40 | 12.00 |
| Mild steel (coated) | 1.08 | 6.51 |
| | | |
| 316 stainless steel (as-supplied) | 0.58 | 3.23 |
| 316 stainless steel (coated) | 0.82 | 5.08 |